Synthesis and evaluation of ^{64}Cu-radiolabeled NOTA-cetuximab (^{64}Cu-NOTA-C225) for immuno-PET imaging of EGFR expression

Xiaoxia Xu[1], Teli Liu[1], Fei Liu[1], Xiaoyi Guo[1], Lei Xia[1], Qing Xie[1], Nan Li[1], Haifeng Huang[1,2], Xianteng Yang[1,2], Yangchun Xin[3], Hua Zhu[1], Zhi Yang[1]

[1]Key Laboratory of Carcinogenesis and Translational Research (Ministry of Education/Beijing), Department of Nuclear Medicine, Peking University Cancer Hospital & Institute, Beijing 100142, China; [2]Department of Orthopaedics, Guizhou Provincial People's Hospital, Guiyang 550002, China; [3]Katzin Diagnostic & Research PET/MR Center, Nemours/Alfred I. DuPont Hospital for Children, Wilmington, DE 19803, USA
Correspondence to: Hua Zhu, PhD. Key Laboratory of Carcinogenesis and Translational Research (Ministry of Education/Beijing), Department of Nuclear Medicine, Peking University Cancer Hospital & Institute, Beijing 100142, China. Email: zhuhuananjing@163.com; Zhi Yang, PhD. Key Laboratory of Carcinogenesis and Translational Research (Ministry of Education/Beijing), Department of Nuclear Medicine, Peking University Cancer Hospital & Institute, Beijing 100142, China. Email: pekyz@163.com.

Abstract

Objective: Epidermal growth factor receptor (EGFR) is overexpressed in a wide variety of solid tumors, serving as a well-characterized target for cancer imaging or therapy. In this study, we aimed to design and synthesize a radiotracer, ^{64}Cu-NOTA-C225, targeting EGFR for tumor positron emission tomography (PET) imaging.

Methods: Cetuximab (C225) was conjugated to a bifunctional chelator, p-isothiocyanatobenzyl-1,4,7-triazacyclononane-1,4,7-triacetic acid (NOTA), and further radiolabeled with copper-64 for PET imaging. ^{64}Cu-NOTA-IgG and Cy5.5-C225 were also synthesized as control probes. A431 and A549 mouse models were established for micro-PET and/or near-infrared fluorescence (NIRF) imaging.

Results: ^{64}Cu-NOTA-C225 exhibited stability *in vivo* and *in vitro* up to 24 h and 50 h post-injection, respectively. A431 tumors with average standard uptake values (SUVs) of 5.61 ± 0.69, 6.68 ± 1.14, 7.80 ± 1.51 at 6, 18 and 36 h post-injection, respectively, which were significantly higher than that of moderate EGFR expressing tumors (A549), with SUVs of 0.89 ± 0.16, 4.70 ± 0.81, 2.01 ± 0.50 at 6, 18 and 36 h post-injection, respectively. The expression levels of A431 and A549 were confirmed by western blotting. Additionally, the tracer uptake in A431 tumors can be blocked by unlabeled cetuximab, suggesting that tracer uptake by tumors was receptor-mediated. Furthermore, NIRF imaging using Cy5.5-C225 showed that the fluorescence intensity in tumors increased with time, with a maximal intensity of $8.17E+10$ $(p/s/cm^2/sr)/(\mu W/cm^2)$ at 48 h post-injection, which is consistent with the paradigm from micro-PET imaging in A431 tumor-bearing mice.

Conclusions: The ^{64}Cu-NOTA-C225 PET imaging may be able to specifically and sensitively differentiate tumor models with different EGFR expression levels. It offers potentials as a PET radiotracer for imaging of tracer EGFR-positive tumors.

Keywords: Epidermal growth factor receptor; immuno-PET imaging; copper-64; monoclonal antibody

Introduction

Epidermal growth factor receptor (EGFR) is expressed in a wide variety of human cancers, including breast cancer, lung cancer, glioblastoma, head and neck cancer, ovarian carcinoma and colorectal cancer (1). Evidence suggests that

EGFR is involved in the pathogenesis and progression of different carcinoma types (2). Of several therapeutic approaches targeting EGFR, inhibition of EGFR with mAbs was the first used in clinical settings (3).

Cetuximab (C225, Erbitux®), a recombinant human/mouse chimeric mAb, binds with the extracellular domain of human EGFR with high affinity and specificity (4-9). It has been approved by the Food and Drug Administration (FDA) for the treatment of patients with EGFR-expressing carcinoma, such as colorectal carcinoma and non-small-cell lung cancer; however, only a subset of patients responds to this treatment (4). The efficacy of cetuximab treatment depends on the level of EGFR expression in the specific tumors of patients. Previously, a clinical study with 1,125 patients suggested that the survival benefit associated with chemotherapy that included cetuximab for non-small-cell lung cancer expressing high levels of EGFR was not limited by EGFR mutation status (10). The expression level of EGFR in most solid tumors was usually determined by immunohistochemistry, fluorescence *in situ* hybridization and gene copy number *ex vivo*; these techniques are invasive, do not account for spatiotemporal heterogeneity, and most notably do not differentiate EGFR expression between primary tumors and metastases. Thus, the current approach to determine the level of EGFR expression within tumors is not sufficient to guide clinical treatment (11,12). More quantitative and reliable methods to measure the expression level of EGFR are required (13). Noninvasive molecular imaging technique to measure tumor EGFR overexpression *in vivo* and to provide more biological information had shown great potential to guide the EGFR-targeting cancer treatment plans (14,15). In this study, we synthesized ^{64}Cu-NOTA-C225; the NOTA chelator was used to connect cetuximab and copper (II) to simplify conjugate production and increase the stability of the copper (II) complex. The stability was evaluated *in vitro* and *in vivo*, and micro-positron emission tomography (micro-PET) imaging was performed in tumor models with different EGFR expression levels.

Materials and methods

General equipment, reagents, cell lines and animal preparation are shown in *Supplementary Table S1*. All animal studies were performed according to a protocol approved by the Animal Care and Use Committee of Peking University Cancer Hospital.

Synthesis, radiolabeling and quality control of ^{64}Cu-NOTA-C225/IgG and Cy5.5-C225

C225/IgG was conjugated to NOTA at a molar ratio of 1:5 at pH 8.4 for 2 h, as previously reported (16). The final products, NOTA-C225 and NOTA-IgG, were purified by PD-10 size-exclusion columns using metal-free phosphate buffer solution (PBS) as the mobile phase to remove unbound NOTA. The molecular weights of the conjugated antibodies (C225, NOTA-C225, IgG and NOTA-IgG) and the number of NOTA chelator molecules per antibody were measured and calculated using matrix-assisted laser desorption ionization time of flight mass spectrometry (MALDI-TOF-MS). For ^{64}Cu radiolabeling, C225/IgG was incubated with ^{64}CuCl$_2$ in 400 μL of sodium acetate buffer (0.1 mol/L, pH 5.5) at room temperature for 20 min (*Figure 1A*). Cy5.5-C225 was synthesized according to reported methods with some modifications (17) (*Supplementary materials*).

In vitro and in vivo stability study

The *in vitro* and *in vivo* stability of ^{64}Cu-NOTA-C225 was measured according to a published method (18,19) (*Supplementary materials*).

Biodistribution and pharmacokinetics study of ^{64}Cu-NOTA-C225 in normal Kunming mice

Two experimental groups of normal Kunming mice were utilized (n=4 for each group). ^{64}Cu-NOTA-C225 (7.4 MBq) was administered via tail vein injection. At 18 and 36 h post-injection, retroorbital blood samples were collected before the normal Kunming mice were sacrificed. All tissues of interest (heart, liver, spleen, lung, kidney, stomach, intestine, bone, muscle and brain) were weighed, and their radioactivity was measured using a γ-counter. The percentage of injected dose per gram of tissue (%ID/g) was calculated by comparison of the radioactivity for each sample with that from a 1:100 diluted standard dose (20). The pharmacokinetics study of ^{64}Cu-NOTA-C225 was performed according to a published procedure (21). Normal Kunming mice (n=4) were used to measure time-radioactivity curves. At various predetermined intervals (1, 3, 5, 10 and 15 min and 0.5, 1, 1.5, 2, 4, 12, 24 and 36 h), 10 μL of blood was drawn from the tail vein, and the radioactivity of each blood sample was measured. The pharmacokinetic parameters were determined by a three-compartment model using GraphPad Prism software (Version 6; GraphPad Software, San Diego, CA, USA).
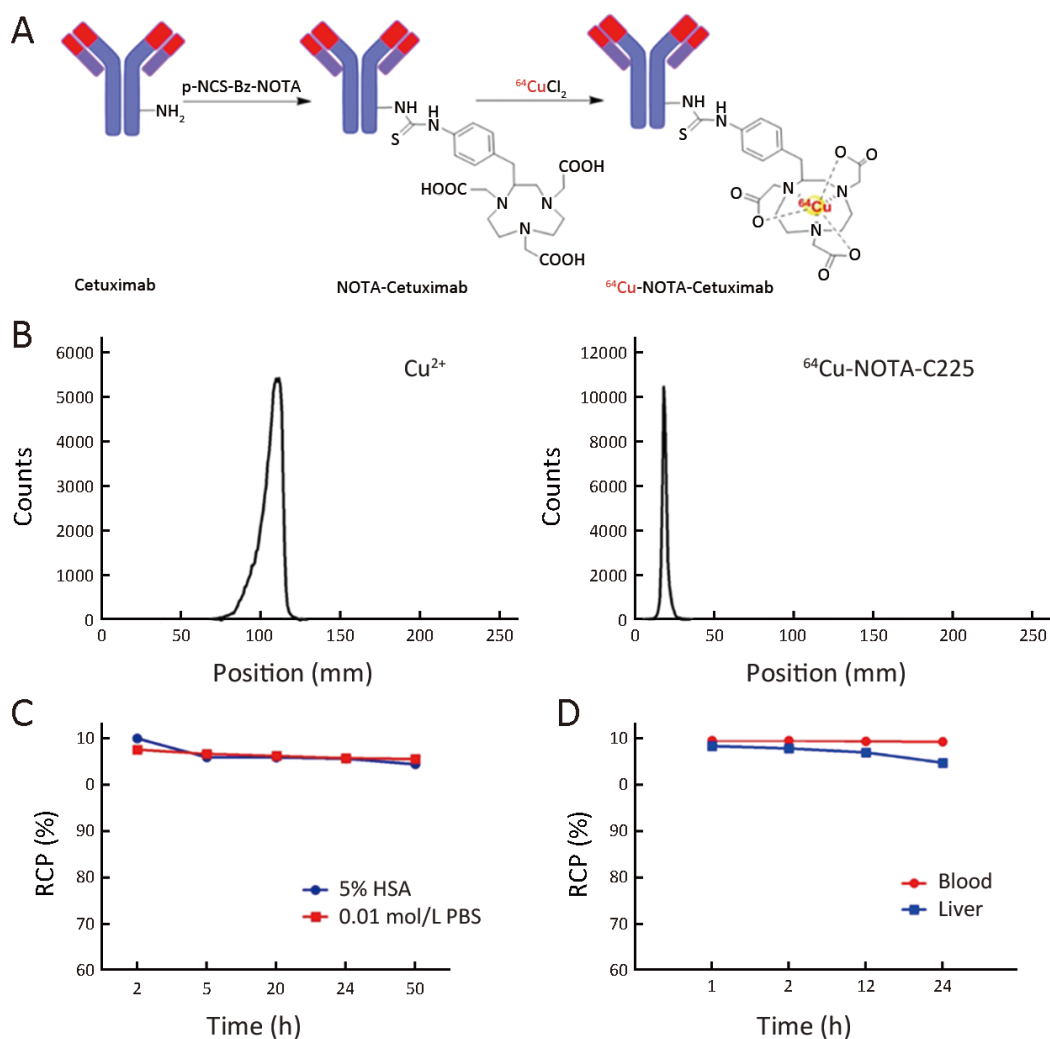
Figure 1 Synthesis of ^{64}Cu-NOTA-C225. (A) Synthetic scheme of ^{64}Cu-NOTA-C225; (B) Instant thin-layer chromatography (ITLC) of Cu^{2+} and ^{64}Cu-NOTA-C225; (C) *In vitro* stability of ^{64}Cu-NOTA-C225 in 0.01 mol/L phosphate buffer solution (PBS) and 5% human serum albumin (HSA); (D) *In vivo* stability of ^{64}Cu-NOTA-C225 in blood and liver.

Micro-PET and near-infrared fluorescence (NIRF) imaging of tumor models with different EGFR expressions

For micro-PET imaging studies, no obesity diabetes and severe combined immune deficiency (NOD-SCID) mice and/or BALB/c nude mice bearing subcutaneously inoculated A431 or A549 xenografts were administered 18.5±0.5 MBq of ^{64}Cu-NOTA-C225/^{64}Cu-NOTA-IgG via tail vein injection (n=4 for each group). Animals were anesthetized with 2.5% isoflurane in 0.5 L/min oxygen flow and maintained with 1.5% isoflurane during the PET scan. Micro-PET imaging was performed on a SuperArgus PET scanner (Sedecal, Spain). Static images were collected at 6, 18 and 36 h post-injection. The images were reconstructed using a three-dimensional ordered subsets expectation maximum algorithm without attenuation correction. The blocking study was performed on A431 tumor-bearing mice (n=3) by co-injection of the radiotracer with cetuximab at the dose of 25 mg/kg. Semi-quantitative analysis of the radioactivity uptake for tumor, heart, liver and muscle, was performed by the average standardized uptake values (SUVs). The SUV was defined as the ratio between the counts per second per pixel in a region of interest (ROI) encompassing the entire organ and the total counts per second per pixel in the mouse (22). The tumor-to-heart (T/H), tumor-to-liver (T/L) and tumor-to-muscle

(T/M) ratios were calculated according to the SUV values.

For NRIF imaging, a Xenogen IVIS^{TM} 200 small animal imaging system with a Cy5.5 filter set (excitation 615 to 655 nm; emission 695 to 770 nm) was used. A431 tumor mice were anesthetized with 2.5% isoflurane and an oxygen flow of 0.5 L/min and maintained in the anesthetized state with 1.0% isoflurane during imaging. Each mouse (n=3) was injected with 1.0 nmol Cy5.5-C225 and was imaged at various time points (2, 24, 48, 72, 96, 160 and 180 h post-injection). All of the fluorescence images were acquired using a 5 s exposure and were normalized by dividing the fluorescence images by the reference illumination images. ROIs were drawn on tumor sites, and the average radiant efficiency [presented as the $\bar{x}\pm s$ in the unit of $(p/s/cm^2/sr)/(\mu W/cm^2)$] within the ROI was used for subsequent quantitative analysis.

Western blotting and autoradiograph

The EGFR expression in A431 and A549 tumor cells was measured using western blotting analysis. Western blotting was performed as described previously (21).

Statistical analysis

Data are expressed as the $\bar{x}\pm s$. GraphPad Prism software was used for statistical analysis. The independent samples *t*-test was used to compare the differences between two quantitative groups with P<0.05 being considered significantly different. * means P<0.05, ** means P<0.01 and *** means P<0.001.

Results

Conjugation of cetuximab

The conjugates, NOTA-C225 and NOTA-IgG, were characterized by MALDI-TOF-MS, and the average number of NOTA chelators attached to each antibody molecule was calculated by the mass difference between the conjugate and starting antibody. The results for NOTA-C225 showed two major peaks centered at 152,663 Da (unconjugated mAb) and 153,141 Da (conjugated mAb). The mass difference equates to an average of 1.0 NOTA group per molecule of cetuximab, and no additional peaks were observed. MALDI-TOF-MS results for NOTA-IgG showed two major peaks centered at 148,066 Da (unconjugated mAb) and 149,651 Da (conjugated mAb). The mass difference equates to an average of 3.3 NOTA groups per molecule of IgG.

Radiosynthesis and quality control of ^{64}Cu-NOTA-C225/IgG

Both ^{64}Cu-NOTA-C225 and ^{64}Cu-NOTA-IgG were obtained with high radiochemical yields (>80%). After purification with a PD-10 column, the radiochemical purities of radiotracers were above 99%. No free ^{64}Cu was found ^{64}Cu-NOTA-C225 (*Figure 1B*) and ^{64}Cu-NOTA-IgG. The specific activity of ^{64}Cu-NOTA-C225/IgG was about 2.96 GBq/μmol.

In vitro and in vivo stability study

Both ^{64}Cu-NOTA-C225 and ^{64}Cu-NOTA-IgG were stable *in vitro* [in both PBS and human serum albumin (HSA)] at 37 °C for more than 50 h (*Figure 1C*). ^{64}Cu-NOTA-C225 was also stable *in vivo* (*Figure 1D*), as determined in the liver and blood of Kunming mice at 1, 2, 12 and 24 h post-injection. These results support that both ^{64}Cu-NOTA-C225 and ^{64}Cu-NOTA-IgG exhibit sufficient stability for preclinical study.

Biodistribution of ^{64}Cu-NOTA-C225 in normal mice

The biodistribution data showed that the liver exhibited relatively moderate uptake of 5.36±0.82 %ID/g at 12 h post-injection and 3.66±0.35 %ID/g at 24 h post-injection. The radioactivity of ^{64}Cu-NOTA-C225 in the liver at 12 h post-injection was significantly lower than that of previously reported ^{64}Cu-DOTA-C225 and ^{64}Cu-PCTA-C225 (the %ID/g was greater than 15 and 12, respectively) (23,24). ^{64}Cu-NOTA-C225 showed moderate blood clearance in normal mice, 6.99±0.96 %ID/g at 18 h post-injection and 5.42±0.36 %ID/g at 36 h post-injection (*Figure 2A*), which is a common feature of intact mAbs (14).

Pharmacokinetics of ^{64}Cu-NOTA-C225 in normal mice

The blood metabolism of ^{64}Cu-NOTA-C225 follows a three-phase decay model as described below (*Figure 2B*):

$Y_{Fast} = (Y0{-}Plateau) \times Percent_{Fast} \times 0.01 \times exp\,({-}K_{Fast} \times X)$

$Y_{Slow} = (Y0{-}Plateau) \times Percent_{Slow} \times 0.01 \times exp\,({-}K_{Slow} \times X)$

$Y_{Medium} = (Y0{-}Plateau) \times (100{-}Percent_{Medium}{-}Percent_{Slow}) \times 0.01 \times exp\,({-}K_{Medium} \times X)$

$Y = Plateau + Y_{Fast} + Y_{Medium} + Y_{Slow}$

Y0 is the Y value when X (time) is zero. Plateau is the Y value at infinite time, expressed in the same units as Y. K_{Fast}, K_{Medium} and K_{Slow} are the rate constants. Half-lives
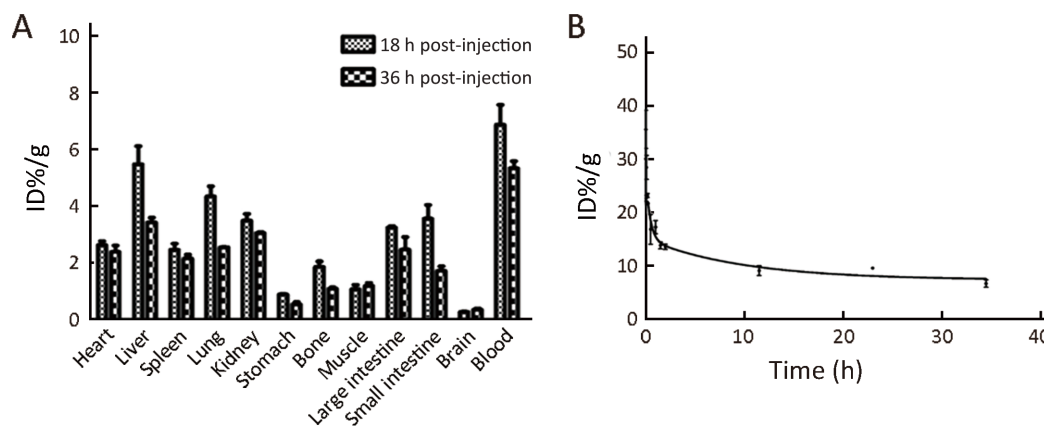
Figure 2 Biodistribution and pharmacokinetics study of ^{64}Cu-NOTA-C225 in normal Kunming mice. (A) Biodistribution of ^{64}Cu-NOTA-C225 in normal Kunming mice at 18 h and 36 h post-injection (n=4); (B) Blood time-radioactivity curve of ^{64}Cu-NOTA-C225 (n=4).

(Fast, Medium and Slow) are computed as the ratio between ln2 and the corresponding rate constants. $Percent_{Fast}$ is the percentage of the area (from Y0 to Plateau) covered by the fastest of the three components. $Percent_{Slow}$ is the percentage of the area (from Y0 to Plateau) covered by the slowest of the three components. The following are equations for ^{64}Cu-NOTA-C225 in normal Kunming mice:

$$Y_{Fast} = (625.7 - 7.374) \times 96.83 \times 0.01 \times exp\,(-246.8 \times X)$$

$$Y_{Slow} = (625.7 - 7.374) \times 1.245 \times 0.01 \times exp\,(-0.1007 \times X)$$

$$Y_{Medium} = (625.7 - 7.374) \times (100 - 96.83 - 1.245) \times 0.01 \times exp\,(-2.318 \times X)$$

The half-lives (Fast, Medium and Slow) were 0.002809, 0.2990 and 6.885 h, respectively.

Micro-PET imaging and autoradiography

The uptake of ^{64}Cu-NOTA-C225 by tumors was significantly higher in the human epidermoid A431 mouse model (high tumor EGFR overexpression) than in the adenocarcinoma A549 mouse model (moderate tumor EGFR overexpression) at all time points (*Figure 3*). The ^{64}Cu-NOTA-C225 uptake in A431 tumors increased steadily over time from 6 to 36 h post-injection (*Figure 3A*), while that in A549 tumors showed moderate uptake at 18 h post-injection only (*Figure 3B*). The expression levels of EGFR in A431 and A549 tumor tissues were also determined *ex vivo* by western blotting (*Figure 3C*) using β-actin protein as the internal standard.

Semi-quantitative analyses of micro-PET tumor images showed that the SUVs of A431 tumors were 5.61±0.69, 6.68±1.14 and 7.80±1.51 at 6, 18 and 36 h, respectively,

while those of A549 tumors were 0.89±0.16, 4.70±0.81 and 2.01±0.50, respectively (*Figure 4A*), with the former always higher than the latter (P<0.01). The SUVs of ^{64}Cu-NOTA-C225 in other major organs in A431 and A549 mice are shown in *Figure 4B,C*. The T/H, T/M and T/L ratios of A431 mice were 3.89±3.82, 9.64±4.26 and 3.05±1.43 at 36 h post-injection, respectively, while those of A549 mice were 0.73±0.29, 0.43±0.35 and 4.34±1.94, respectively (*Figure 4D*). The radioactivity uptake values for the non-specific radioligand ^{64}Cu-NOTA-IgG in A431 tumors were significantly lower than those for the specific radioligand ^{64}Cu-NOTA-C225 at each time point (*Figure 5A,B*), supporting the specific binding of ^{64}Cu-NOTA-C225 within tumors. Moreover, when excess cetuximab was co-injected with the specific radioligand ^{64}Cu-NOTA-C225, the tumor radioactivity uptake was significantly reduced in A431 tumors, with overall PET images matching those of the non-specific radioligand ^{64}Cu-NOTA-IgG (*Figure 5A,B*). The specific binding of ^{64}Cu-NOTA-C225 in tumors observed by PET images was further confirmed by autoradiography *ex vivo* (*Figure 5C*).

NIRF imaging of Cy5.5-C225 in A431 xenotransplantation mice

In vivo fluorescence imaging over extended time periods showed that Cy5.5-C225 gradually accumulated in A431 tumors transplanted into NOD-SCID mice at 0, 24, 48 and 72 h post-injection (*Figure 6A*). When the fluorescence intensities in tumors were plotted against time post-injection, a bell-shaped curve with maximal intensity [8.17E+10(p/s/cm^2/sr)/(μW/cm^2)] at 48 h post-injection appears (*Figure 6B*). When both time-activity curves of
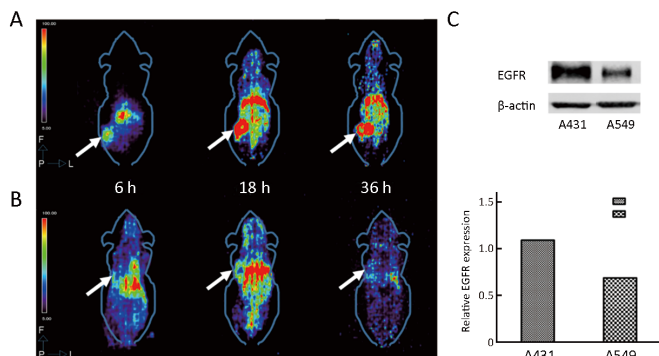
Figure 3 Micro-positron emission tomography (Micro-PET) of tumor models with different epidermal growth factor receptor (EGFR) expressions. (A) Micro-PET images of ^{64}Cu-NOTA-C225 in A431 xenograft no obesity diabetes and severe combined immune deficiency (NOD-SCID) mice at 6, 18 and 36 h after injection; (B) Micro-PET images of ^{64}Cu-NOTA-C225 in A549 xenograft NOD-SCID mice at 6, 18 and 36 h after injection. White arrows indicate tumor; (C) Relative EGFR expressions in A431 (left column) and A549 cancer cells (right column), and representative EGFR expressions were presented as the ratios of EGFR *vs*. β-actin expressions by western blotting analysis.

PET imaging and fluorescence imaging were combined, the general patterns match each other, each confirming the conclusion of the other (*Figure 6C*).

Discussion

The development of EGFR-targeted molecular probes is greatly needed to measure the level of EGFR expression and the heterogeneity of different lesions *in vivo*. The retrospective analysis of a large randomized trial study showed that non-small-cell lung carcinoma patients with high tumor EGFR expression would most likely benefit from the addition of cetuximab to platinum-based first-line chemotherapy, independently of tumor histology (25). Cetuximab antibody blocks the natural ligand from binding to EGFR, leading to a decrease in receptor dimerization, autophosphorylation and activation of signaling pathways (26). EGFR protein expression has the potential to serve as a biomarker to predict favorable outcomes from cetuximab administration in multiple cancer types. However, it is rather disappointing that the methods for the detection of EGFR positivity as well as other potential biomarkers are by no means standardized, which necessitates substantial improvements (27). The mainstream method to detect EGFR expression in tumors is to analyze the EGFR RNA

in tumor tissue samples collected from surgery or puncture. However, the spatiotemporal heterogeneity of EGFR in tumor tissue cannot be analyzed. This limits the application of the *in vitro* measurement of EGFR (28). In addition, Laskin *et al*. (29) found evidence to demonstrate that the quantification of EGFR by immunohistochemistry is also unreliable.

With this study, we are the first to report ^{64}Cu-NOTA-C225 as a micro-PET imaging radioligand in human epidermoid (A431) and adenocarcinoma (A549) mouse models. The critical feature of our ^{64}Cu-NOTA-C225 radioligand is *in vivo* and *in vitro* stability. Previous studies indicated that ^{64}Cu labeled DOTA-cetuximab showed promise for PET imaging of EGFR-positive tumors; however, *in vivo* instability of this compound was observed (30). It has been established that DOTA is not the ideal chelator for ^{64}Cu. Bifunctional chelators bearing cross-bridged macrocycles demonstrate much greater stability with ^{64}Cu, such as 2,2'-[1,4,8,11-tetraazabicyclo (6.6.2) hexadecane-4,11-diyl] diacetic acid, and can reduce copper (II) dissociation and non-specific copper (II) uptake (31). Unfortunately, the radiolabeling requires harsher labeling conditions (95 °C for 60 min and pH greater than 8) (32,33), which are incompatible for proteins.

We selected NOTA as the linker to synthesize ^{64}Cu-NOTA-C225 as our radioligand. ^{64}Cu-NOTA-C225 is convenient for radiolabeling and stable both *in vitro* and *in vivo*. The complete radiolabeling required only 20 min at room temperature, and the ^{64}Cu-NOTA-C225 product is stable *in vitro* and *in vivo* for up to 50 h/24 h; this stability is sufficient for application in clinical studies. The radioactivity uptake of ^{64}Cu-NOTA-C225 in the liver was significantly lower than that of previously reported ^{64}Cu-DOTA-C225 and ^{64}Cu-PCTA-C225 (%ID/g was above 15 and 12, respectively) (23,24), which supports the observation of decreased dissociation of copper (II) from the radioligand *in vivo*.

The anti-EGFR antibodies radiolabeled with technetium-99m, indium-111, lutetium-177 and zirconium-89 have been studied previously (13,34,35). ^{64}Cu is a beneficial and favorable radionuclide among the other copper radionuclides, as it emits low energy positrons with the endpoint energy of 653 keV and average energy of 278 keV. This radionuclide is also characterized by a medium energy beta particle, gamma radiation and an appropriate half-life ($t_{1/2}$=12.7 h), allowing the combination of PET scan with diagnosis and radiotherapy (36). Our
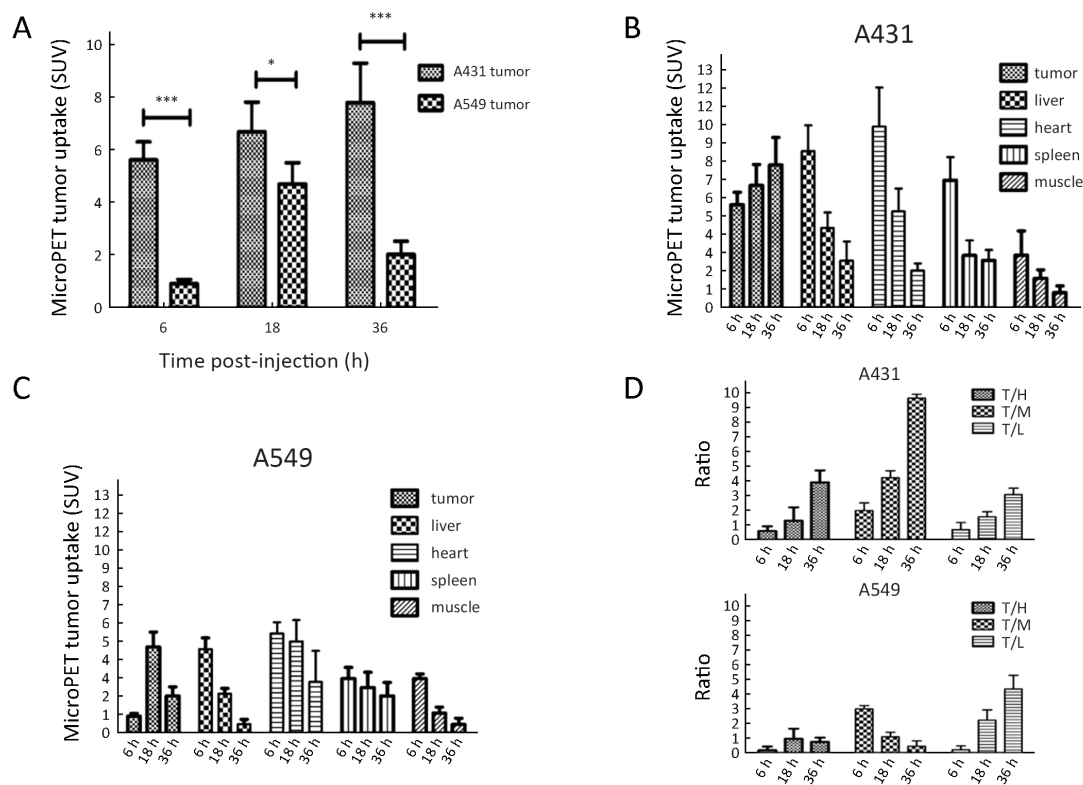
Figure 4 Semi-quantitative analyses of micro-positron emission tomography (micro-PET) images. (A) Comparison of the tumor radioactivity uptake of 64Cu-NOTA-C225 standard uptake value (SUV) between A431 and A549 tumors; (B) SUV of 64Cu-NOTA-C225 in A431 tumors and major organs; (C) SUV of 64Cu-NOTA-C225 in A549 tumors and major organs; (D) Tumor-to-heart (T/H), tumor-to-liver (T/L) and tumor-to-muscle (T/M) of 64Cu-NOTA-C225 in A431 and A549 mice. All data were represented as $\bar{x} \pm s$ (n=4).

result showed that micro-PET imaging using 64Cu-NOTA-C225 can measure EGFR expression in tumor models. For the EGFR-overexpressing tumor, A431, the PET signal gradually increases within the tumor at 6, 18 and 36 h post-injection. However, for the moderate EGFR-expressing tumor, A549, tracer uptake by the tumor was lower at all time points. The amount of EGFR expression was measured *ex vivo* by western blotting, confirming that the EGFR expression in A431 is much greater than that in A549. A similar paradigm was observed in the Cy5.5-C225 fluorescence imaging probe study.

Conclusions

We have synthesized a new radioligand, 64Cu-NOTA-C225, with high chemical and radiochemical yield and purity. The radioligand displays sufficient *in vitro/vivo* stability. PET imaging with 64Cu-NOTA-C225 showed that the radioligand can specifically and sensitively bind with EGFR receptors in EGFR-positive tumors. This

study demonstrates the potential of 64Cu-NOTA-C225 for further clinical application in patients with EGFR-overexpressing tumors and proper selection of patients for cetuximab therapy, monitoring the effects of therapies, following disease progression, and eventually enabling individualized treatment.

Footnote

Conflicts of Interest: The authors have no conflicts of interest to declare.
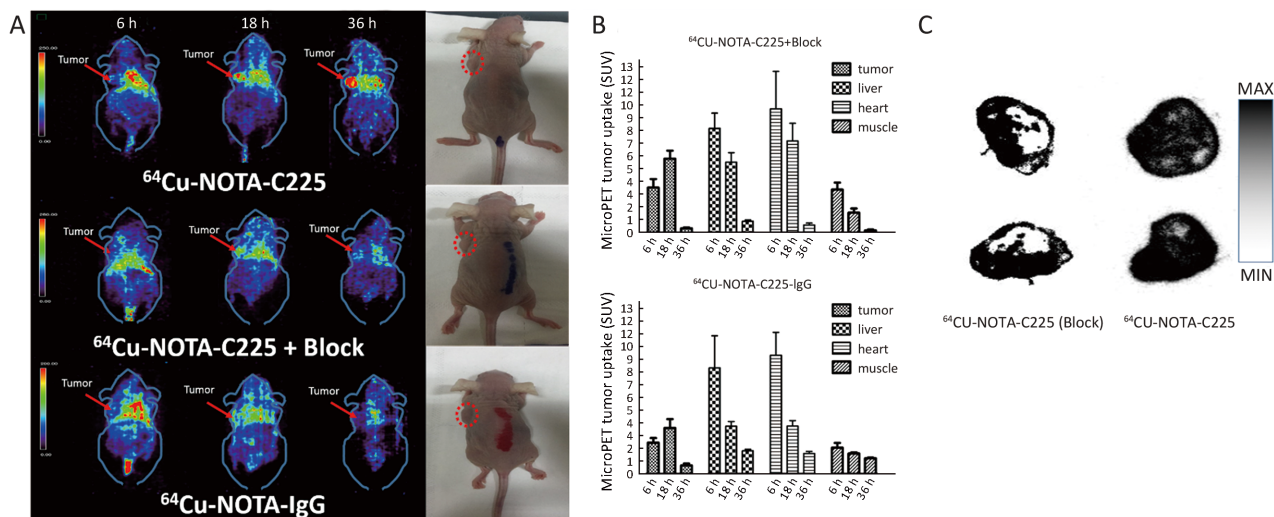
Figure 5 Micro-positron emission tomography (Micro-PET) imaging and autoradiography. (A) Micro-PET images of ^{64}Cu-NOTA-C225, ^{64}Cu-NOTA-C225 + Block and ^{64}Cu-NOTA-IgG in A431 xenograft nude mice at 6, 18 and 36 h post injection; (B) Standard uptake values (SUVs) of specific radioligand ^{64}Cu-NOTA-C225 + Block and those of non-specific radioligand ^{64}Cu-NOTA-IgG; (C) Autoradiography images of tumor sections (25 µm) obtained from A431 tumor 60 h after injection with and without blocking.
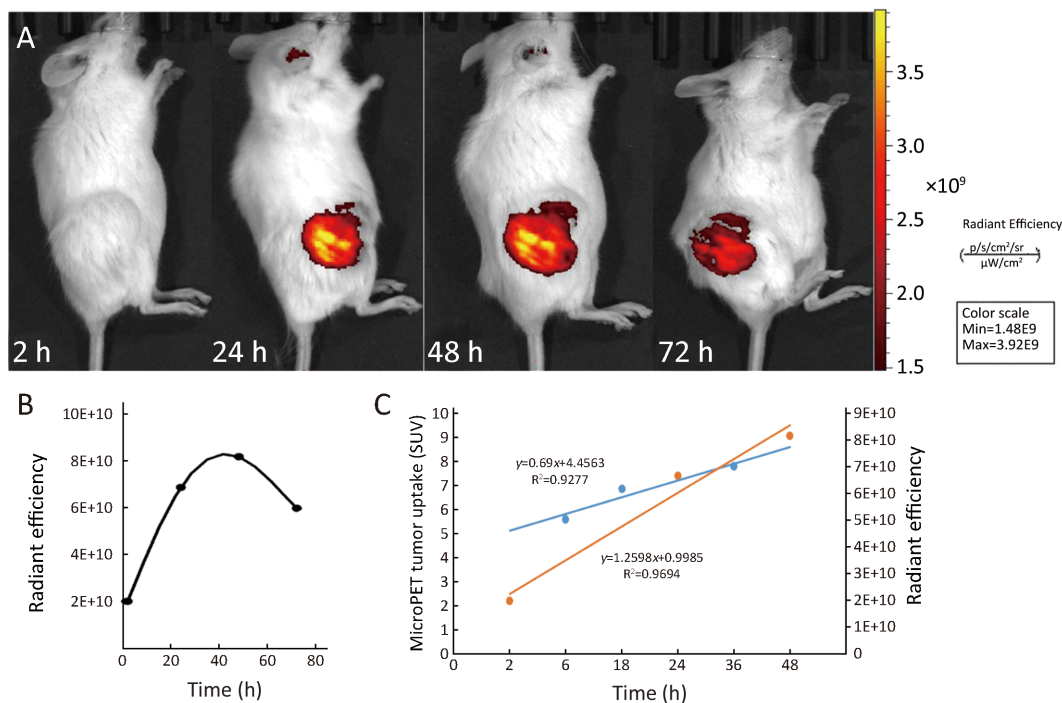

Figure 6 Near-infrared fluorescence (NIRF) imaging of Cy5.5-C225 and semi-quantitative analyses. (A) NIRF of Cy5.5-C225 in A431 xenograft mice; (B) Radiant efficiency curve of tumors changed over time in optical imaging; (C) Semi-quantitative analysis of micro-positron emission tomography (micro-PET) tumor uptake (blue line) and optical radiant efficiency in A431 tumors (red line).

References

1. Wendt MK, Williams WK, Pascuzzi PE, et al. The anti-tumorigenic function of EGFR in metastatic breast cancer is regulated by expression of Mig6. Neoplasia 2015;17:124-33.

2. Normanno N, De Luca A, Bianco C, et al. Epidermal growth factor receptor (EGFR) signaling in cancer. Gene 2006;366:2-16.

3. Grünwald V, Hidalgo M. The epidermal growth factor receptor: a new target for anticancer therapy. Curr Probl Cancer 2002;26:109-64.

4. Wong SF. Cetuximab: an epidermal growth factor receptor monoclonal antibody for the treatment of colorectal cancer. Clin Ther 2005;27:684-94.

5. Cunningham D, Humblet Y, Siena S, et al. Cetuximab monotherapy and cetuximab plus irinotecan in irinotecan-refractory metastatic colorectal cancer. N Engl J Med 2004;351:337-45.

6. Saltz LB, Meropol NJ, Loehrer PJ Sr, et al. Phase II trial of cetuximab in patients with refractory colorectal cancer that expresses the epidermal growth factor receptor. J Clin Oncol 2004;22:1201-8.

7. Poston G, Adam R, Xu J, et al. The role of cetuximab in converting initially unresectable colorectal cancer liver metastases for resection. Eur J Surg Oncol 2017;43:2001-11.

8. Guren TK, Thomsen M, Kure EH, et al. Cetuximab in treatment of metastatic colorectal cancer: final survival analyses and extended RAS data from the NORDIC-VII study. Br J Cancer 2017;116:1271-8.

9. Wang L, Wei Y, Fang W, et al. Cetuximab enhanced the cytotoxic activity of immune cells during treatment of colorectal cancer. Cell Physiol Biochem 2017;44:1038-50.

10. Douillard JY, Pirker R, O'Byrne KJ, et al. Relationship between EGFR expression, *EGFR* mutation status, and the efficacy of chemotherapy plus cetuximab in FLEX study patients with advanced non-small-cell lung cancer. J Thorac Oncol 2014;9:717-24.

11. Italiano A, Follana P, Caroli FX, et al. Cetuximab shows activity in colorectal cancer patients with tumors for which FISH analysis does not detect an increase in EGFR gene copy number. Ann Surg Oncol 2008;15:649-54.

12. Lenz HJ, Van Cutsem E, Khambata-Ford S, et al. Multicenter phase II and translational study of cetuximab in metastatic colorectal carcinoma refractory to irinotecan, oxaliplatin, and fluoro-pyrimidines. J Clin Oncol 2006;24:4914-21.

13. Perk LR, Visser GW, Vosjan MJ, et al. 89Zr as a PET surrogate radioisotope for scouting biodistribution of the therapeutic radiometals 90Y and 177Lu in tumor-bearing nude mice after coupling to the internalizing antibody cetuximab. J Nucl Med 2005;46:1898-906.

14. Niu G, Li Z, Xie J, et al. PET of EGFR antibody distribution in head and neck squamous cell carcinoma models. J Nucl Med 2009;50:1116-23.

15. Mishani E, Abourbeh G, Eiblmaier M, et al. Imaging of EGFR and EGFR tyrosine kinase overexpression in tumors by nuclear medicine modalities. Curr Pharm Des 2008;14:2983-98.

16. Guleria M, Das T, Amirdhanayagam J, et al. Comparative evaluation of using NOTA and DOTA derivatives as bifunctional chelating agents in the preparation of 68Ga-labeled porphyrin: impact on pharmacokinetics and tumor uptake in a mouse model. Cancer Biother Radiopharm 2018;33:8-16.

17. Li N, Zhu H, Li Y, et al. Synthesis and evaluation of Cy5.5-Rit tracer for specific near-infrared fluorescence imaging of sentinel lymph node. Bioorg Med Chem Lett 2016;26:4233-6.

18. Bansal A, Pandey MK, Demirhan YE, et al. Novel 89Zr cell labeling approach for PET-based cell trafficking studies. EJNMMI Res 2015;5:19.

19. Mou T, Zhao Z, Fang W, et al. Synthesis and preliminary evaluation of 18F-labeled pyridaben analogues for myocardial perfusion imaging with PET. J Nucl Med 2012;53:472-9.

20. Han XD, Liu C, Liu F, et al. 64Cu-PSMA-617: A novel PSMA-targeted radio-tracer for PET imaging in gastric adenocarcinoma xenografted mice model. Oncotarget 2017;8:74159-69.

21. Liu F, Liu T, Xu X, et al. Design, synthesis, and biological evaluation of 68Ga-DOTA-PA1 for lung cancer: A novel PET tracer for multiple somatostatin receptor imaging. Mol Pharm 2018;15:619-28.

22. Ping Li W, Meyer LA, Capretto DA, et al. Receptor-binding, biodistribution, and metabolism studies of 64Cu-DOTA-cetuximab, a PET-imaging agent for epidermal growth-factor receptor-positive tumors. Cancer Biother Radiopharm 2008;23:158-71.

23. Guo Y, Parry JJ, Laforest R, et al. The role of p53 in combination radioimmunotherapy with 64Cu-DOTA-cetuximab and cisplatin in a mouse model of colorectal cancer. J Nucl Med 2013;54:1621-9.

24. Song IH, Lee TS, Park YS, et al. Immuno-PET

imaging and radioimmunotherapy of [64]Cu-/177Lu-labeled anti-EGFR antibody in esophageal squamous cell carcinoma model. J Nucl Med 2016;57:1105-11.

25. Losanno T, Rossi A, Maione P, et al. Anti-EGFR and antiangiogenic monoclonal antibodies in metastatic non-small-cell lung cancer. Expert Opin Biol Ther 2016;16:747-58.

26. Zhang Y, Yang J, Ding M, et al. Tumor-penetration and antitumor efficacy of cetuximab are enhanced by co-administered iRGD in a murine model of human NSCLC. Oncol Lett 2016;12:3241-9.

27. Patil N, Abba M, Allgayer H. Cetuximab and biomarkers in non-small-cell lung carcinoma. Biologics 2012;6:221-31.

28. Dai D, Li XF, Wang J, et al. Predictive efficacy of 11C-PD153035 PET imaging for EGFR-tyrosine kinase inhibitor sensitivity in non-small cell lung cancer patients. Int J Cancer 2016;138:1003-12.

29. Laskin JJ, Sandler AB. Epidermal growth factor receptor: a promising target in solid tumours. Cancer Treat Rev 2004;30:1-17.

30. Boswell CA, Sun X, Niu W, et al. Comparative *in vivo* stability of copper-64-labeled cross-bridged and conventional tetraazamacrocyclic complexes. J Med Chem 2004;47:1465-74.

31. Wadas TJ, Wong EH, Weisman GR, et al. Copper chelation chemistry and its role in copper radiopharmaceuticals. Curr Pharm Des 2007;13:3-16.

32. Sprague JE, Peng Y, Sun X, et al. Preparation and biological evaluation of copper-64-labeled tyr3-octreotate using a cross-bridged macrocyclic chelator. Clin Cancer Res 2004;10:8674-82.

33. Wadas TJ, Anderson CJ. Radiolabeling of TETA- and CB-TE2A-conjugated peptides with copper-64. Nat Protoc 2006;1:3062-8.

34. England CG, Jiang D, Hernandez R, et al. ImmunoPET imaging of CD146 in murine models of intrapulmonary metastasis of non-small cell lung cancer. Mol Pharm 2017;14:3239-47.

35. Goldenberg A, Masui H, Divgi C, et al. Imaging of human tumor xenografts with an indium-111-labeled anti-epidermal growth factor receptor monoclonal antibody. J Natl Cancer Inst 1989;81:1616-25.

36. Karimi Z, Sadeghi M, Mataji-Kojouri N. [64]Cu, a powerful positron emitter for immunoimaging and theranostic: Production via [nat]ZnO and [nat]ZnO-NPs. Appl Radiat Isot 2018;137:6-61.

Supplementary materials

Materials and methods

Western blotting, autoradiography and hematoxylin-eosin (HE) staining

The epidermal growth factor receptor (EGFR) expression in A431 and A549 tumor cells was measured using western blotting analysis. First, the isolated tissues were homogenized by mechanical disruption to obtain the total protein. The protein concentrations were determined using a bicinchoninic acid (BCA) Protein Assay Kit (Biosynthesis Biotechnology, Beijing, China). Equal amounts of protein lysates (5 μL) were loaded and separated by sodium dodecyl sulfate-polyacrylamide gel electrophoresis (SDS/PAGE), and the separated proteins were transferred into polyvinylidene fluoride (PVDF) membranes, which were blocked using 5% nonfat milk dissolved in TBST solution for 1 h at room temperature. Membranes were then probed with polyclonal rabbit anti-human anti-EGFR (ab52894) (1:1,000) or monoclonal mouse anti-β-actin antibody (1:5,000) at 4 °C overnight. After washing with TBST three times, the membranes were incubated with a goat anti-rabbit (1:20,000) secondary antibody labeled with horseradish peroxidase for 1 h at room temperature. The chemiluminescent signals were captured with the Odyssey Fc Imaging System (LI-COR Biosciences, Lincoln, NE).

For autoradiography, the A431 tumor tissues were cut into slices (25.0 μm thick) on a cryostat (Cryo-Star HM 560 MV, Microm). The tumor slices were exposed to a phosphorus plate (Perkin-Elmer, USA) for 24 h. Then, the autoradiograph images were obtained using a phosphor imaging system (Cyclone, Packard).

For HE staining, the A431 tumor tissue was fixed in a fresh 10% formaldehyde-mixing fixative for 24 h, rehydrated, embedded in paraffin and cut into slices (25.0 μm thick) on a cryostat. These sections were processed by a standardized hematoxylin and eosin staining method according to manufacturers' protocols, and the images were obtained under a microscope.

Mass spectrometry analysis of cetuximab/IgG and modified cetuximab/IgG

The samples were diluted to 1.0 μg/mL with 0.01 mol/L phosphate buffer solution (PBS). Sinapinic acid was dissolved in an acetonitrile/water/trifluoroacetic acid (TFA) (50/50/0.1) solution to a concentration of 15.0 mg/mL, and this solution was used for matrix-assisted laser desorption ionization (MALDI): 1.0 μL of solution containing a 1:1 mixture of sample and matrix was used for mass analysis. The spectrum was acquired in positive linear mode and analyzed using Flex Analysis v3.0 software (Bruker Daltonics, Bremen, Germany).

Preparation and purification of Cy5.5-C225 conjugates

Briefly, cetuximab (4.0 mg) in 500 μL of 0.1 mol/L sodium bicarbonate (NaHCO$_3$) buffer (pH=8.2) was mixed with 0.3 mg of Cy5.5-NHS in 30 μL of dimethylformamide (DMF) at 0 °C. The reaction vial was wrapped with aluminum foil, and the mixture was allowed to warm to room temperature (25 °C) with stirring for 2 h. The reaction solution must avoid light during the reaction. The product, Cy5.5-C225, was purified by a PD-10 column.

In vitro and *in vivo* stability study

Briefly, the radiolabeled compound (64Cu-NOTA-C225/IgG) was incubated in 0.01 mol/L PBS (pH=7.4) or 5% human serum albumin (HSA) at 37 °C for 0.5, 1, 12, 18 and 36 h. The radiochemical purities of the radiotracers were analyzed by instant thin-layer chromatography (ITLC) and high-performance liquid chromatography (HPLC).

The *in vivo* stability was studied during 24 h after injection. Blood and liver were collected and analyzed. Briefly, the blood sample was immediately centrifuged for 5 min at 13,200 r/min. The liver was homogenized and suspended in 1 mL of methanol and then centrifuged for 5 min at 13,000 r/min. The liver and blood supernatants were collected and analyzed by ITLC.

Table S1 Materials and origins

Materials	Origin
^{64}Cu	$^{64}Ni(p, n)^{64}Cu$ reaction with a specific activity of 5.6 GBq/μmol at Beijing Cancer Hospital using the HM-20 cyclotron
Cetuximab	Merck KGaA (Darmstadt, GER)
PD-10 Desalting Columns	GE Healthcare (Fairfield, CT, USA)
MALDI-TOF-MS	Bruker (Bruker Daltonics, USA)
HPLC (Agilent Technologies 1200)	Agilent Technologies (California, USA)
ITLC-SG (silica gel) strips	Agilent Technologies (Lake Forest, CA, USA)
AR-2000 Radio-TLC Imaging Scanner	Washington, DC, USA
A431 (human epidermal carcinoma) cells	China infrastructure of cell line resources
A549 (adenocarcinoma human alveolar basal epithelial) cells	China infrastructure of cell line resources
BALB/c nude mice, normal Kunming mice and NOD-SCID mice	Beijing Huafukang (HFK) Bioscience Co. Ltd. (Beijing, China)

MALDI-TOF-MS, matrix-assisted laser desorption ionization time of flight mass spectrometry; NOD-SCID, no obesity diabetes and severe combined immune deficiency.